EnvironmentAsia
The international journal by the Thai Society of Higher Education Institutes on Environment

EnvironmentAsia 17(2) 2024 78-90
DOI 10.14456/ea.2024.22
ISSN 1906-1714; ONLINE ISSN: 2586-8861

Rapid Monitoring of Flood Events in Geothermal Surrounding Areas Using Machine Learning and Multi-sensor Data

Fahmi Arif Kurnianto*, Elan Artono Nurdin, Era Iswara Pangastuti, and Moch Ilham Deka Rafsanjani

Department of Geography Education, University of Jember, Jember, Indonesia

*Corresponding author: fahmiarif.fkip@unej.ac.id
Received: October 14, 2023; Revised: December 5, 2023; Accepted: January 26, 2024

Abstract

Volcano arcs, particularly the Sunda Arc, are predominant in Indonesia and constitute a key tectonic system in current geodynamics, making it essential for several stakeholders to consider geothermal exploration while taking into account the environmental impact. In previous reports, conventional methods were used in mapping environmental impact zones, leading to inefficiency in the monitoring process. Therefore, this study aimed to monitor flood in geothermal surrounding areas using machine learning and multisensor data. In the process, sentinel 1 GRD was adopted to map flood area distribution and was compared to Sentinel 2 optic data. Furthermore, Google Earth Engine was used to process several steps, including acquisition, polarization, measuring indices, and post-processing. Mapping was conducted at flooded areas in Ciwidey and Pasirjambu as geothermal surroundings. The results showed that flooded areas were located in the built-up areas as a part of watershed downstream. Ciwidey District had a wider flooded area than Pasirjambu. In June 2022, VH polarization of flooded areas in Ciwidey was recorded at -25, correlating with field data. Meanwhile, the comparison between VH polarization in Pasirjambu and Sentinel 2 indicated that flooded areas were associated with low NDVI and SAVI values, representing low infiltration. Google Earth Engine was capable of detecting several areas with different topography through optical and SAR data fusion. Differences in flood detection were discovered between VH and VV polarizations in the subset area around geothermal area. VH polarization was more accurate for detecting flood distribution due to the capability to acquire inundation data in densely vegetated areas. Additionally, the method can be used to distinguish permanent water bodies in the form of lakes/craters from flood inundations. This study concluded that machine learning and multi-sensor data facilitated the mapping and monitoring of flood distribution using both temporal analysis and a faster process.

Keywords: Rapid monitoring; Flood; Machine learning; Multi Sensor Data

1. Introduction

Indonesia is a nation constituting 13% of the world's volcanoes, leading to an enormous geothermal potential. Geothermal exploration in the country is inherently challenging due to complex topography and dense vegetation. The identification of geothermal manifestation requires preliminary steps, such as mapping mineral alteration on the surface (Cumming, 2009; Pirajno, 2009; Stelling *et al.,* 2016). The process of mapping the surface to identify alteration has been successfully implemented using remote sensing, particularly in areas with sparse vegetation. However, this method faces limitations when applied in areas characterized by dense vegetation.

Traditionally, optical imagery has been widely used to map the characteristics of the earth surface, including mineral alteration

(van der Meer *et al.,* 2014). Landsat 8 and Sentinel 2 images provide optical data, but images have limitations for mapping in the tropical area. Several previous studies effectively adopted optical imagery to map surface alteration in semi-arid areas, such as Nevada, United States (Coolbaugh *et al.* 2007, Ninomiya 2004), and the African Desert (Aboelkhair *et al.* 2020; Gabr *et al.,* 2015; Madani and Emam 2011).

Geothermal manifestations in tropical areas are related to vulnerabilities, such as mass movement, land cover change, and flood disasters. These areas are frequently designated as conservation zones, requiring careful consideration of factors like geology, soil composition, rainfall patterns, and land cover to ensure sustainable geothermal energy development. Previous studies by Gemitzi *et al.* (2021), Weldeyohannes *et al.* (2022), and Yanis *et al.* (2023) explored geothermal detection using remote sensing data, focusing on anomalies in land surface temperature. Other studies by Horn *et al.* (2022) and Ioannou *et al.* (2023) investigated the relationship between geothermal installations and social conflict.

According to Handayani & Singarimbun (2016), the South Bandung area, including Ciwidey, often experiences landslide and flood due to the pyroclastic nature of the bedrock and geothermal exploration activities. Supporting this, Bronto & Hartono (2006) stated that the entire Bandung Basin area, including Ciwidey, was highly vulnerable to flood. Consequently, when engaging in natural resources exploration, specifically geothermal, environmental consideration becomes essential. Based on additional reports by Usman *et al.* (2020), geothermal exploration in Ciwidey can lead to changes in land use changes, presenting the necessity for ecological studies to prevent flood. Ciwidey and Pasirjambu lie in the Quaternary volcanic zone, characterized by hilly topography, high rainfall, and unstable pyroclastic bedrock vulnerable to exogenous processes. Given the ongoing geothermal exploration in this area, conducting studies focused on monitoring flood disasters becomes crucial.

In the context of integrating remote sensing with in situ data, several studies from Isa *et al.* (2020), Abubakar (2019), and Zhao *et al.* (2023) showed the relationship between geothermal, as well as geological patterns and structures, which are also associated with surface mineral alteration. The reports examined the mapping of the geological structure, essential for understanding fracture, alteration, and magma distribution. Another aspect examined by Zaini *et al.* (2023) and Okoroafor *et al.* (2023) demonstrated the applicability of machine-learning algorithms for mapping geothermal potential. Flood mapping in geothermal areas is conducted after a disaster using radar and optical data. In this study, it aims to capture real-time events, including the distribution of affected areas and the relationship with various environmental aspects, such as vegetation.

These previous studies examined geothermal in the context of exploration and the impact on the surrounding environment. However, there remains a gap in investigations regarding environmental monitoring due to geothermal installations using machine learning. Therefore, the novelty of this study lies in the development of a rapid monitoring system integrating multi-sensor data and machine learning to improve flood model mapping in surrounding areas of geothermal installations through time series analysis. The report assumes significance as continuous monitoring of the environmental impact of geothermal energy is essential, and recommendations should be provided to developers related to corporate social responsibility (CSR). The objectives to be performed include monitoring flood events around geothermal exploration of surrounding areas and using machine learning, incorporating optic data and synthetic aperture radar, to rapidly map flood areas.

2. Methodology

2.1 Data selection and pre-processing

This study used Sentinel-1 Synthetic Aperture Radar (SAR) data collected from COPERNICUS/S1, on July 6, 2022, through GEE. The data had a spatial resolution of 10 m, and a series of pre-processing steps were implemented, including thermal noise removal

and radiometric calibration. Furthermore, the collection process was conducted before and after flood events. Sentinel-1 level 1 GRD, with geometry projected onto the WGS 84 ellipsoid, was adopted for the reliability. Following pre-processing, filtering was performed by considering the type of polarization. This study was specifically conducted in Ciwidey and Pasirjambu Districts of West Java due to significant geothermal explorations in the Upstream Area.

These areas often experience large-scale flood. To conduct flood mapping on 6 June 2022, Sentinel 1 SAR data was complemented by Sentinel 2 optical data. Cloud masking techniques were applied on the Google Earth Engine platform, as recommended by (Mateo-García et al., 2018), to ensure the acquisition of cloud-free images. Median filtering was subsequently adopted for each pixel to produce a clear composite image of the entire study area (Wang et al., 2018; Zurqani et al., 2018). Mapping surface characteristics, such as land cover or surface water, in mountainous areas, requires SAR capabilities, exemplified by Sentinel 1, to obtain a clear image that can penetrate through the cloud (Flores-Anderson et al., 2019; Kim et al., 2011; Huang et al., 2017).

2.2 Multisensor data

To accurately capture and analyze flood events, Sentinel 1 radar data and Sentinel 2 optic data were used, a particularly effective approach in tropical areas with high-intensity rainfall. Sentinel 2, with a spatial resolution of 10 m and a temporal resolution of 5 days, facilitated the mapping of vegetation and water indices. Furthermore, the optical data served as a valuable comparative reference to the radar data. Sentinel 1 effectively maps flood distribution due to its capability to detect the Earth's surface in various weather conditions at a relatively high resolution (Wakabayashi et al., 2019). With a temporal resolution of 6 days and a spatial resolution of 5 m, it not only provides valuable insights into flood patterns but also allows for the display of topographic data in the study area through Sentinel 1 on Google Earth Engine (GEE). This satellite series proves adept at detecting floods as historical events by adopting specified temporal parameters (Priyatna et al., 2023). For the 'before flood' analysis in this study, data from January 2021 was utilized, while post-flood imaging in June 2021 relied on the Sentinel-1 picture mosaic.Several aspects comprising the input of the study area, the date when flood occurred, and identified water and non-water pixels, were used to determine flood areas (Islam & Meng, 2022).

2.3 Machine learning

Random Forest and threshold algorithms were used to map flood events rapidly. Random Forest detected several land classes due to the ability to process data with regression and parallel implementation. In this study, RF was trained to differentiate land classes based on the reflectance value of each class by using the Google Earth Engine platform (https://earthengine.google.com/). Furthermore, it uses trees hj (X,θj) as the base learners (Sakti *et al.,* 2023). The training data, D = {(x1, y1),….., (xN,yN)}, where xi = (x1, j, . . . , xi,p), T denotes the p predictors, y1 denotes the response, and hj(x, θj, D) denotes the realization for θj. The RF algorithm, expressed in Equation 1, sets the predictions for Sentinel 2A.

$$f(x) = argmax_y \sum_{j=1}^{J} I(h_j(x) = y) \qquad (1)$$

To map vegetation indices, NDVI was applied through Sentinel 2 data:

$$NDVI = \frac{\rho_{NIR} - \rho_{Red}}{\rho_{NIR} + \rho_{Red}} \qquad (2)$$

Where ρRed is the reflectance in the red band and ρNIR is the reflectance in the near-infrared band. Clouds were identified by the QA information. Subsequently, the gaps were filled backward in time as the data quality was better in more recent years (Yu *et al.,* 2021). The following represented scale coefficient, k, calculated to minimize the bias:

$$NDVI_{rec} = NDVI_{pred} \times k \qquad (3)$$

NDVIpred was applied to predict the NDVI time series. Following adjustment, NDVIrec was used as a final reconstructed

NDVI time series. Additionally, SAVI was used to confirm the instability of NDWI output and reduced soil brightness through the red (RED) and NIR wavelengths (Huete *et al.,* 1988). The SAVI index is represented by Equation 4:

$$SAVI = ((NIR - RED)/(NIR + RED + L)) \times (1 + L) \quad (4)$$

Where L adjusts the canopy background, with a value of 0.5 was selected to mitigate variation in soil brightness and eliminate the need for additional calibration in different soil types (Qi *et al.,* 1994).

2.4 Threshold

Identifying flood areas requires an optimum threshold value. Pixel values of interest (POI), such as water and cities, were extracted from the ratio index value of change detection results. Training data, generated interactively by digitizing Google Earth Engine, is used to establish optimal threshold values for various land cover classes. POI data was then superimposed on SAR image resulting from the change detection process for statistical calculations. The determination of the optimum threshold includes the application of the equation proposed by (Vanama, *et al.,* 2021). Flood areas were identified using a threshold value derived from the pixel value of POI. Finally, samples for the training area were used to produce the optimum threshold value.

2.5 Change detection

To identify inundation, a ratio image technique was used to compare the ratio of the backscattering coefficient values before and when a flood occurs (Awaliyah & Hariantaka, 2021). The ratio value greater or less than 1 indicates changes in the area. Bright colors in the image signify high pixel values with substantial changes, while dark colors denote low pixel values with minimal changes. Several optic data sources, including NDVI, SAVI, and Composite at Sentinel 2, were adopted for spectral index comparison.

2.6 Backscatter

The spectral characteristics were determined by the combination of environmental factors and radar system parameters (Zhang *et al.,* 2021). In this context, both spectral and backscatter characteristics were closely related. SAR backscatter coefficients were influenced by several variables, including the dielectric constant of the target, SAR wavelength, image acquisition geometry, local geography, and surface roughness. To assess the sensitivity of different polarizations in water areas, a comparison is made using VV and VH polarizations. Additionally, to mitigate noise in the backscatter feature, a band combination is performed by constructing radar indexes based on differences and ratios. The study flowchart is presented in Figure 1.

3. Results and Discussion

The comparison between optical and radar data is beneficial for monitoring results. This is because radar data effectively complements the weaknesses of optical data, particularly cloud cover and topography. Figures 2A and 2B show the distribution of flooded areas in built-up areas featuring a low vegetation index. These areas, located on a flat slope, are predominantly occupied by settlements with respective NDVI scores ranging from 0.0 - 0.35. Additionally, Figure 2C indicates SAVI values in the range of 0 - 0.1, respectively, suggesting a dominance of non-vegetation classes in the area. Figure 2D shows flood areas with a dark hue. This result was in line with Parks *et al.* (2018), which detected soil deformation in Reykjanes, Iceland, leading to increased surface runoff. Land subsidence between 5 mm and 20 mm per year in Iceland alters morphology, making it more susceptible to flood (Vasco *et al.,* 2013; Drouin *et al.,* 2017).

The identification of flood in areas with flat topography is attributed to the area in downstream watersheds. Figure 3A shows that flooded areas are concentrated in downstream areas characterized by a flat topography. The area in Ciwidey District is wider than Pasirjambu District, indicating a relatively

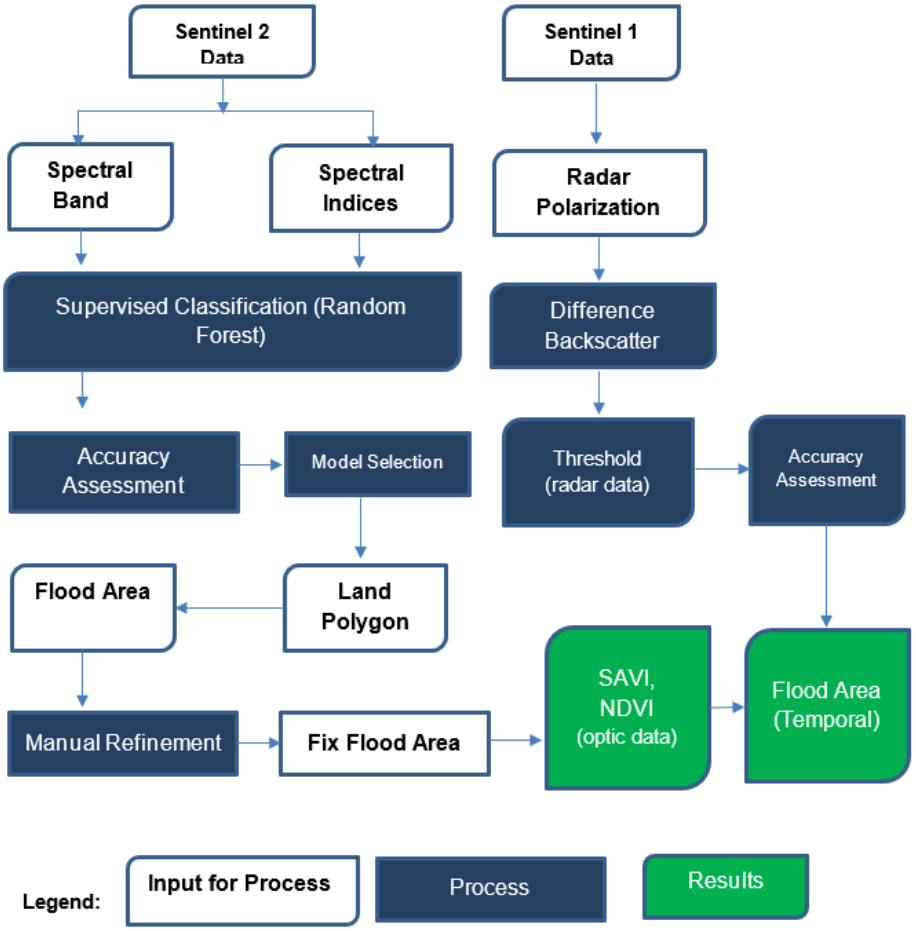

Figure 1. Research Flowchart

high loss to the community. Based on Figures 2B and 2C, the most affected areas had low vegetation index values. Figure 3A presents the superior capability of SAR data over optical data in detecting flood areas around geothermal installations. The optical data represented by the NDVI, SAVI, and Sentinel 2 Composite methods is limited to detecting vegetation and non-vegetation. The results were in line with several studies related to SAR imagery processing that surface deformation and infiltration characteristics was detected with InSAR (e.g., Amelung *et al.,*1999; Bell *et al.,* 2008; Castellazzi *et al.,* 2018). According to the reports, most of the affected areas were in urban settings (e.g., Brunori *et al.,* 2015; Chaussard *et al.,* 2014; Cigna *et al.,* 2012a; Pacheco-Martínez *et al.,* 2015) despite environmental damage extending to various areas (Figueroa-Miranda *et al.,* 2018).

A comparison of VV and VH polarization in radar data has been conducted quickly over the same area to test the validity of the mapping. In Figure 5A, VH polarization in the proximity of geothermal area demonstrates a more accurate relief of flood areas, as evidenced by the ability to distinguish between permanent water bodies (lakes or craters) and flood inundations. Figure 5B presents the superior accuracy of VH polarization compared to VV polarization (Figures 5C and 5D). VH polarization does not classify the lake/crater as flood inundation. Figure 5 also presents the difference in the distribution of flooded areas between the results of VV and VH polarization. VH polarization detects wider flood in the southern part of the area. This result was supported by the study of Guan *et al.* (2023), that polarization was more accurate in detecting inundation in areas with dense vegetation.

Given the high vegetation density around geothermal area, VH polarization proves effective at identifying larger flood areas. Additionally, a previous study by Grimadi et al. (2020) presented the accuracy of polarization alongside several algorithms for detecting flood.

Flood monitoring around geothermal areas needs to consider vegetation index fluctuations. Figure 6 shows that the temporal vegetation index is at a high value of 0.8, respectively. A high index indicates that the area around geothermal installation can overcome potential waste pollution. Furthermore, flood incidents in residential areas were not directly related to geothermal exploration. The original NDVI values was reported to be in the range of 0.7 – 0.8, representing that the area around geothermal exploration has not experienced significant changes in vegetation. The observation was in line with Figure 4, presenting the high distribution of vegetation density in the area closest to geothermal installation.

The temporal vegetation index in Figure 6 confirms that flood inundation in nearby areas occurs on a small scale and does not pose the risk of mass movement at present. This result was supported by several previous studies by Huang *et al.* (2018), which demonstrated the capability of SVM algorithm in detecting landslides in geothermal areas through field validation. Hong *et al.* (2018) succeeded in mapping mass movement hazards in geothermal areas using decision trees. The results of these studies were complemented, particularly in monitoring flood and runoff quickly.

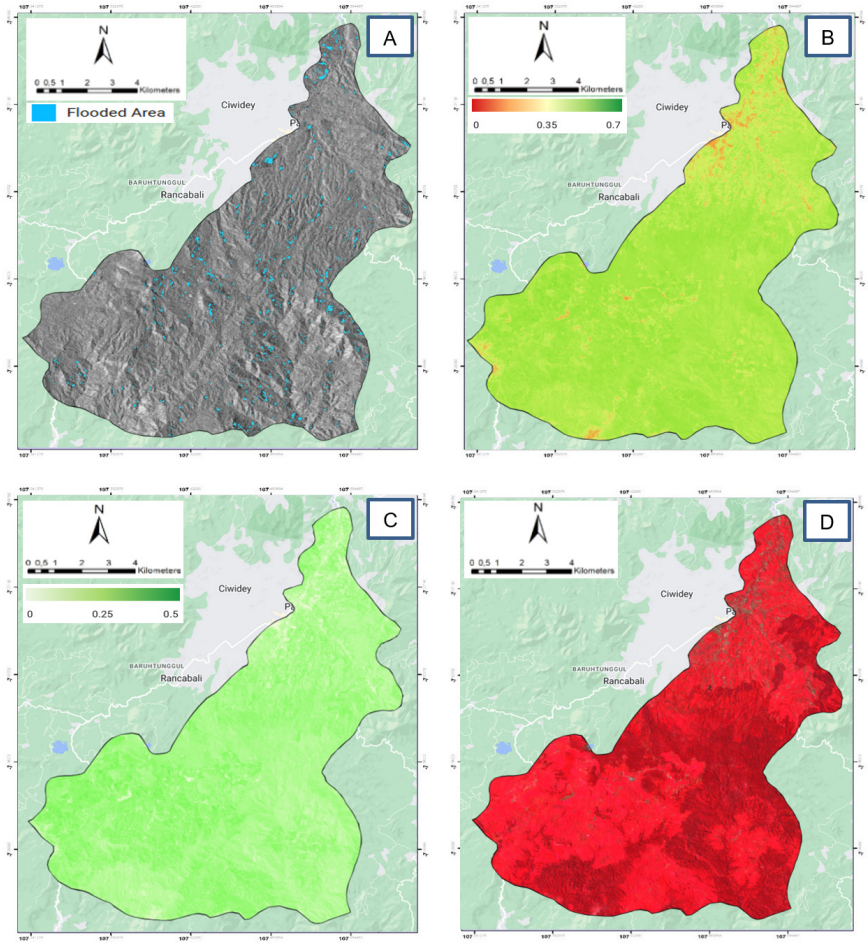

Figure 2. Pasirjambu District, A: Flooded Area Mapping by Sentinel 1, B: NDVI Map by Sentinel 2, C: SAVI Map by Sentinel 2, D: Sentinel 2 Composite

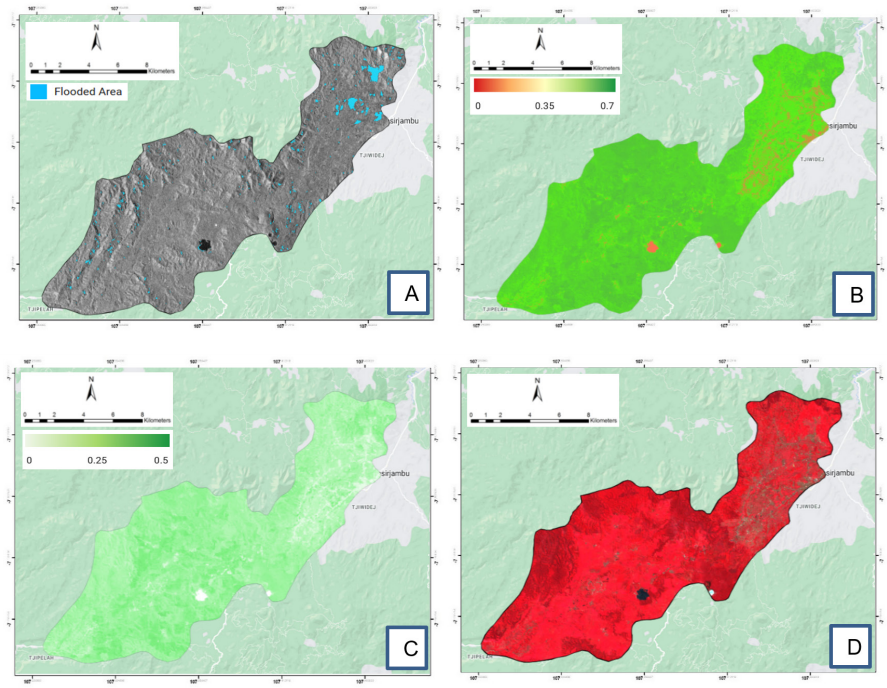

Figure 3. Ciwidey District , A : Flooded Area Mapping by Sentinel 1, B: NDVI Map by Sentinel 2, C: SAVI Map by Sentinel 2, D : Sentinel 2 Composite

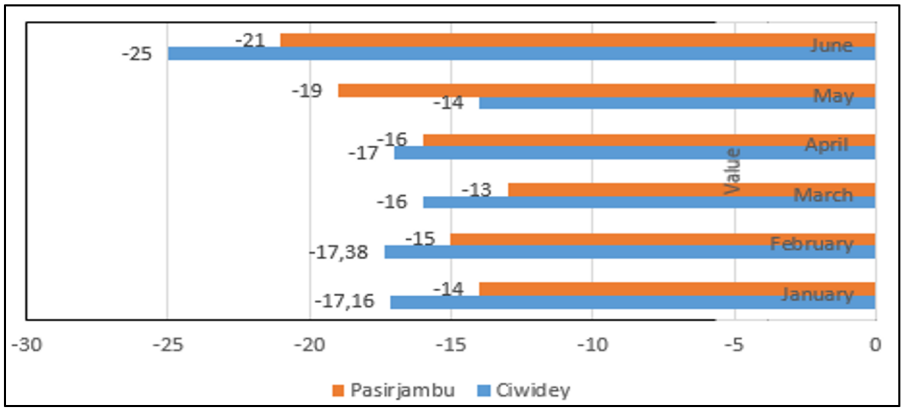

Figure 4. Time series VH Polarization in Pasirjambu and Ciwidey (2022)

The highest accuracy among algorithms was observed in the threshold method applied to VH polarization, with a User and Producer Accuracy of 92.6% and 86.3% respectively. In contrast, Sentinel 2 (random forest) optical data, achieved User and Producer Accuracies of 83.6% and 88.2%. The results showed that both radar and optic data were capable of detecting flood areas and the relationship to vegetation indices such as SAVI and NDVI. The accuracy test used a purposive sampling method, comprising a total of 64 flood areas. Table 1 presents a confusion matrix detailing the sensor and algorithm comparison, along with accuracy assessments.

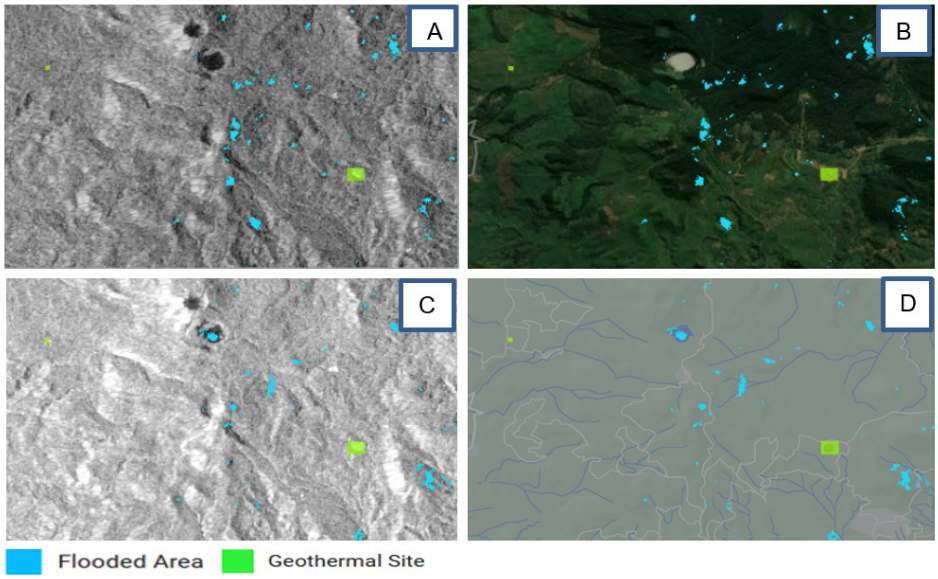

Figure 5. Geothermal nearest area , A : VH Polarization at Flooded Area by Sentinel 1, B: VH Polarization at Flooded Area in Google Earth Satellite, C: VV Polarization at Flooded Area by Sentinel 1, D : VV Polarization at Flooded Area in Google Map

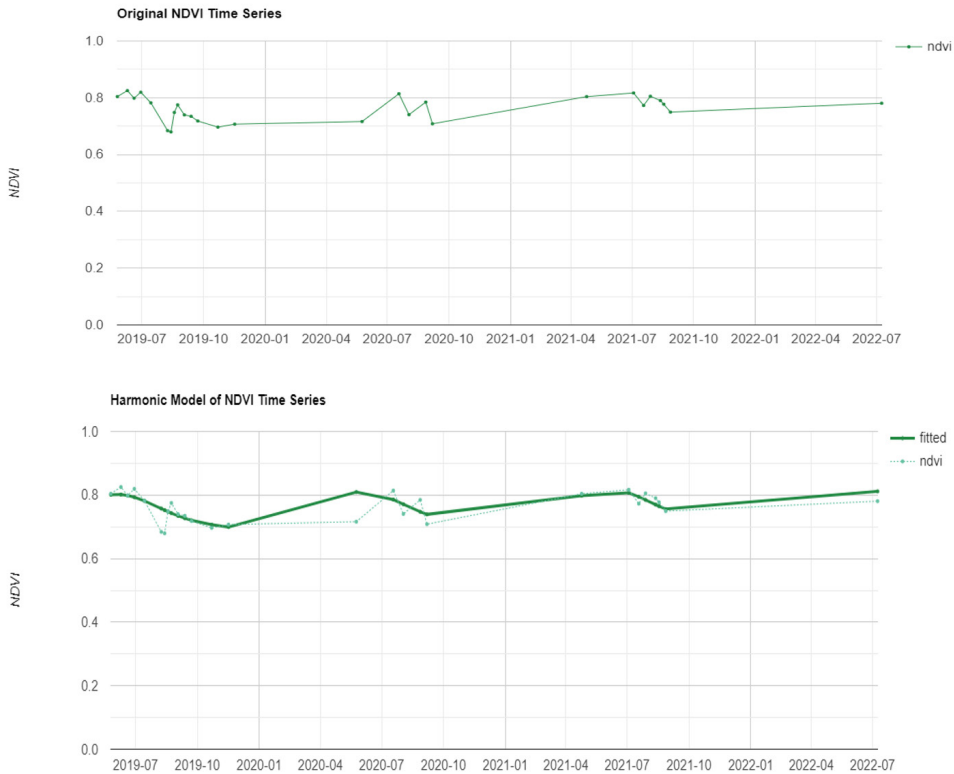

Figure 6. Original NDVI and Harmonic Model of NDVI Time series at study area

Table 1. Confusion matrix

Sensor	Algorithm	User Accuracy (%)	Producer Accuracy (%)
VH Polarization	Threshold	92.6	86.3
VV Polarization	Threshold	71.2	83.3
Sentinel 2	Random Forest	83.6	88.2

This study shows that flood in Ciwidey and Pasirjambu occurred significantly after geothermal exploration. The result was in line with the report of Zhang *et al.* (2016), demonstrating the close relationship between geothermal energy and natural disasters such as landslide, debris flow, and flood. The affected area, characterized by a flatter topography compared to others, accumulated all mass movements and floods into Ciwidey and Pasirjambu. This phenomenon is supported by Wilopo & Fathani (2021), showing that the mass movement mechanism in a geothermal area is influenced by alteration processes affecting clay mineral presence. As part of the quaternary volcanic landscape, these areas have thick soil layers, resulting in the accumulation of clay minerals due to rainwater. Figure 4 shows runoff in the study area, indicating the potential for debris flow in the upstream area closest to geothermal exploration. This was in line with the study of Permanda & Ohtani (2020), demonstrating that the injection process impacts the potential for debris and flood. According to Fathani *et al.* (2022), the upstream area had the highest level of erosion, capable of causing mass movement and flood in downstream areas.

The inundation shown in Figure 4 presents the potential for debris flow in the upstream area closest to geothermal exploration. This result is supported by a study from Permanda & Ohtani (2020), indicating that the injection process in geothermal exploration impacts the potential for debris and flood. According to Fathani *et al.* (2022), the upstream area has the highest level of erosion, capable of causing mass movement and flood in downstream areas.

4. Conclusion

In conclusion, the rapid detection of flood event in June 2022 around geothermal area was made possible through the use of machine learning and multisensor data. SAR data played a crucial role in mapping flood in areas with high cloud cover. Optical data served as a valuable comparative tool, indicating that the majority of flood distribution occurred in built-up areas. Machine learning demonstrated the capability to rapidly discern temporal inundation changes, presenting a substantial difference in VH polarization before and during flood. VH polarization, particularly in extensive inundated zones, had a significant increase. Additionally, this approach proved effective in identifying flood-prone areas with high-density vegetation in geothermal surroundings. It is important to note that the area closest to geothermal area remained unaffected by large-scale runoff or flood from 2019 to 2022. The results showed the efficiency of mapping using machine learning, outpacing conventional methods devoid of the technological advancements. The algorithm, with the ability to accurately identify areas affected by flood, is particularly valuable during the disaster. This study presents the expeditious resolution of cloud cover challenges commonly encountered in geothermal areas by leveraging algorithms and GEE platform. Consequently, the combination of machine learning and multisensor data was a viable alternative to traditional methods, specifically in geothermal areas where data acquisition limitations persisted.

References

Aboelkhair H, Abdelhalim A, Hamimi Z, Al-Gabali M. Reliability of using ASTER data in lithologic mapping and alteration mineral detection of the basement complex of West Berenice, Southeastern Desert, Egypt. Arabian Journal of Geosciences 2020; 13.

Abubakar AJA, Hashim M, Pour AB. Remote sensing satellite imagery for prospecting geothermal systems in an aseismic geologic setting: Yankari Park, Nigeria. International Journal of Applied Earth Observation and Geoinformation 2019; 80:157-172.

Alawiyah AM, Harintaka H. Identifikasi Genangan Banjir di Wilayah DKI Jakarta Menggunakan Citra Satelit Sentinel-1. JGISE: Journal of Geospatial Information Science and Engineering 2021; 4(2): 95-101.

Amelung F, Galloway DL, Bell JW, Zebker HA, Laczniak RJ. Sensing the ups and downs of Las Vegas: InSAR reveals structural control of land subsidence and aquifer-system deformation. Geology 1999; 27(6): 483-486.

Bell JW, Amelung F, Ferretti A, Bianchi M, Novali F. Permanent scatterer InSAR reveals seasonal and long-term aquifer-system response to groundwater pumping and artificial recharge. Water Resources Research 2008. 44(2).

Bronto S, Hartono U. Potensi sumber daya geologi di daerah Cekungan Bandung dan sekitarnya. Indonesian Journal on Geoscience 2006; 1(1): 9-18.

Browne PRL. Hydrothermal alteration in active geothermal fields. Annu. Rev. Earth Planet. Sci. 1978; 6: 229–248.

Brunori CA, Bignami C, Albano M, Zucca F, Samsonov S, Groppelli G, Norini G, Saroli M, Stramondo S. Land subsidence, ground fissures and buried faults: InSAR monitoring of Ciudad Guzmán (Jalisco, Mexico). Remote Sensing 2015; 7(7): 8610-8630.

Castellazzi P, Longuevergne L, Martel R, Rivera A, Brouard C, Chaussard E. Quantitative mapping of groundwater depletion at the water management scale using a combined GRACE/InSAR approach. Remote Sensing of Environment 2018; 205: 408-418.

Chaussard E, Wdowinski S, Cabral-Cano E, Amelung F. Land subsidence in central Mexico detected by ALOS InSAR time-series. Remote sensing of environment 2014; 140: 94-106.

Cigna F, Osmanoğlu B, Cabral-Cano E, Dixon TH, Ávila-Olivera JA, Garduño-Monroy VH, DeMets C, Wdowinski, S. Monitoring land subsidence and its induced geological hazard with Synthetic Aperture Radar Interferometry: A case study in Morelia, Mexico. Remote Sensing of Environment 2012; 117: 146-161.

Drouin V, Sigmundsson F, Verhagen S, Ófeigsson BG, Spaans K, Hreinsdóttir, S. Deformation at krafla and bjarnarflag geothermal areas, northern volcanic zone of iceland, 1993–2015. Journal of Volcanology and Geothermal Research 2017; 344: 92-105.

Fathani TF, Wilopo W, Amalina AN, Pramaditya A. Debris flow hazard analysis toward the implementation of mitigation measures. GEOMATE Journal 2022; 23(95): 45-56.

Figueroa-Miranda S, Tuxpan-Vargas J, Ramos-Leal JA, Hernández-Madrigal V M, & Villaseñor-Reyes CI. Land subsidence by groundwater over-exploitation from aquifers in tectonic valleys of Central Mexico: A review. Engineering Geology 2018; 246: 91-106.

Flores-Anderson AI, Herndon KE, Thapa RB, Cherrington E. The SAR handbook: Comprehensive methodologies for forest monitoring and biomass estimation (No. MSFC-E-DAA-TN67454) 2019.

Freski YR, Hecker C, Van der Meijde M, Setianto, A. The effects of alteration degree, moisture and temperature on laser return intensity for mapping geothermal manifestations. Geothermics 2021; 97: 102250.

Gabr SS, Hassan SM, Sadek MF. Prospecting for new gold-bearing alteration zones at El-Hoteib area, South Eastern Desert, Egypt, using remote sensing data analysis. Ore Geol. Rev 2015; 71:1–13. https://doi.org/10.1016/J.OREGEOREV.2015.04.021.

Gemitzi A, Dalampakis P, Falalakis G. Detecting geothermal anomalies using Landsat 8 thermal infrared remotely sensed data. International Journal of Applied Earth Observation and Geoinformation 2021; 96: 102283.

Grimaldi S, Xu J, Li Y, Pauwels VR, Walker JP. Flood mapping under vegetation using single SAR acquisitions. Remote sensing of Environment 2020; 237: 111582.

Guan H, Huang J, Li L, Li X, Miao S, Su W, Ma Y, Quandi N, Huang, H. Improved Gaussian mixture model to map the flooded crops of VV and VH polarization data. Remote Sensing of Environment 2023; 295: 113714.

Handayani L, Singarimbun, A. Pemetaan Daerah Rawan Longsor di Sekitar Daerah Prospek Panas Bumi Provinsi Jawa Barat. Journal Online of Physics 2016; 2(1): 17-22.

Hong H, Liu J, Bui DT, Pradhan B, Acharya TD, Pham BT, Zhu A, Chen W, Ahmad BB. Landslide susceptibility mapping using J48 Decision Tree with AdaBoost, Bagging and Rotation Forest ensembles in the Guangchang area (China). Catena 2018; 163: 399-413.

Horn D, Gross M, Pfeiffer M, Sonnberger M. How far is far enough? The social constitution of geothermal energy through spacing regulations. Sustainability 2022; 14(1): 496.

Huang W, DeVries B, Huang C, Lang MW, Jones JW, Creed IF, Carroll ML. Automated extraction of surface water extent from Sentinel-1 data. Remote Sensing 2018; 10(5): 797.

Huang Y, Zhao, L. Review on landslide susceptibility mapping using support vector machines. Catena 2018; 165: 520-529.

Huete AR. A soil-adjusted vegetation index (SAVI). Remote sensing of environment 1988; 25(3): 295-309.

Ioannou A, Falcone G, Baisch C, Friederichs G, Hildebrand JA. Decision support tool for social engagement, alternative financing and risk mitigation of geothermal energy projects. Energies 2023; 16(3): 1280.

Isa M, Cesarian DP, Abir IA, Yusibani E, Surbakti MS, Umar, M. Remote Sensing Satellite Imagery and In-Situ Data for Identifying Geothermal Potential Sites: Jaboi, Indonesia. International Journal of Renewable Energy Development 2020; 9(2): 237-245.

Islam MT, Meng, Q. An exploratory study of Sentinel-1 SAR for rapid urban flood mapping on Google Earth Engine. International Journal of Applied Earth Observation and Geoinformation 2022; 113: 103002.

Kim Y, Jackson T, Bindlish R, Lee H, Hong S. Radar vegetation index for estimating the vegetation water content of rice and soybean. IEEE Geoscience and Remote Sensing Letters 2011; 9(4): 564-568.

Madani AA, Emam AA. SWIR ASTER band ratios for lithological mapping and mineral exploration: a case study from El Hudi area, southeastern desert, Egypt. Arab. J. Geosci 2011; 4: 45–52.

Mateo-García G, Gómez-Chova L, Amorós-López J, Muñoz-Marí J, Camps-Valls, G. Multitemporal cloud masking in the Google Earth Engine. Remote Sensing 2018; 10(7): 1079.

Okoroafor ER, Smith CM, Ochie KI, Nwosu CJ, Gudmundsdottir H, Aljubran, MJ. Machine learning in subsurface geothermal energy: Two decades in review. Geothermics 2022; 102: 102401.

Pacheco-Martínez J, Cabral-Cano E, Wdowinski S, Hernández-Marín M, Ortiz-Lozano JÁ, Zermeño-de-León ME. Application of InSAR and gravimetry for land subsidence hazard zoning in Aguascalientes, Mexico. Remote Sensing 2015; 7(12): 17035-17050.

Parks M, Sigmundsson F, Sigurðsson Ó, Hooper A, Hreinsdóttir S, Ófeigsson B, Michalczewska K. Deformation due to geothermal exploitation at Reykjanes, Iceland. Journal of Volcanology and Geothermal Research 2020; 391: 106438.

Permanda R, Ohtani T. Environmental Impact of Open-Loop Geothermal Heat Pumps System on the Nagara River Alluvial Fan in Gifu City, Central Japan. In Proceedings World Geothermal Congress 2020; 1.

Pirajno F. Hydrothermal processes and wall rock alteration. Hydrothermal Processes and Mineral Systems. Springer Science+Business Media 2009; 73–164.

Priyatna M, Khomarudin MR, Wijaya SK, Yulianto F, Nugroho G, Afgatiani PM, Rarasati A, Hussein MA. Rapid Flood Mapping Using Statistical Sampling Threshold Based on Sentinel-1 Imagery in the Barito Watershed, South Kalimantan Province, Indonesia. Journal of Engineering & Technological Sciences 2023; 55(1).

Priyatna M, Wijaya SK, Khomarudin MR, Yulianto F, Nugroho G, Afgatiani PM, Rarasati A, Hussein MA. The use of multi-sensor satellite imagery to analyze flood events and land cover changes using change detection and machine learning techniques in the Barito watershed. Journal of Degraded & Mining Lands Management 2023; 10(2).

Qi J, Chehbouni A, Huete AR, Kerr YH, Sorooshian SA. Modified soil adjusted vegetation index. Remote sensing of environment 1994; 48(2): 119-126.

Rahman MS, Di L. A systematic review on case studies of remote-sensing-based flood crop loss assessment. Agriculture 2020; 10(4): 131.

Sakti AD, Sembiring E, Rohayani P, Fauzan KN, Anggraini TS, Santoso C, Patricia VA, Ihsan KTN, Ramadan AH, Arjasakusuma S, Candra, DS. Identification of illegally dumped plastic waste in a highly polluted river in Indonesia using Sentinel-2 satellite imagery. Scientific Reports 2023; 13(1): 5039.

Stelling P, Shevenell L, Hinz N, Coolbaugh M, Melosh G, Cumming W. Geothermal systems in volcanic arcs: volcanic characteristics and surface manifestations as indicators of geothermal potential and favorability worldwide. J. Volcanol. Geotherm. Res. 2016; 324: 57–72.

Stroppiana D, Boschetti M, Azar R, Barbieri M, Collivignarelli F, Gatti L, Fontanellli G, Busetto L, Holecz, F. In-season early mapping of rice area and flooding dynamics from optical and SAR satellite data. European Journal of Remote Sensing 2019; 52(1): 206-220.

Uddin K, Matin MA, Meyer FJ. Operational flood mapping using multi-temporal Sentinel-1 SAR images: A case study from Bangladesh. Remote Sensing 2019; 11(13): 1581.

Usman DN, Widayati S, Sriyanti S. Geological based on area development: terrain genetic unit method. Journal of Physics: Conference Series 2020;1469(1).

Vasco DW, Rutqvist J, Ferretti A, Rucci A, Bellotti F, Dobson, P, Oldenburg C, Garcia J, Walters M, Hartline, C. Monitoring deformation at the Geysers Geothermal Field, California using C-band and X-band interferometric synthetic aperture radar. Geophysical Research Letters 2013; 40(11): 2567-2572.

Wakabayashi H, Motohashi K, Kitagami T, Tjahjono B, Dewayani S, Hidayat D, Hongo C. Flooded area extraction of rice paddy field in Indonesia using Sentinel-1 SAR data. The International Archives of the Photogrammetry, Remote Sensing and Spatial Information Sciences 2019; 42: 73-76.

Wang C, Jia M, Chen N, Wang, W. Long-term surface water dynamics analysis based on Landsat imagery and the Google Earth Engine platform: A case study in the middle Yangtze River Basin. Remote Sensing 2018; 10(10): 1635.

Weldeyohannes TT, Hailu BT, Muluneh AA, Kidane T. Detection of geothermal anomalies in the Northern Lake Abaya geothermal field, Main Ethiopian Rift. Journal of Volcanology and Geothermal Research 2022; 430: 107638.

Wilopo W, Fathani TF. The mechanism of landslide-induced debris flow in geothermal area, Bukit Barisan mountains of Sumatra, Indonesia. Journal of Applied Engineering Science 2021; 19(3): 688-697.

Yanis M, Zaini N, Novari I, Abdullah F, Dewanto BG, Isa M, Marwan M, Zainal, M, Abdurrahman A. Monitoring of Heat Flux Energy in the Northernmost Part of Sumatra Volcano Using Landsat 8 and Meteorological Data. International Journal of Renewable Energy Development 2023; 12(1): 55-65.

Yu W, Li J, Liu Q, Zhao J, Dong Y, Zhu X, Lin S, Zhang H, & Zhang, Z. Gap filling for historical landsat ndvi time series by integrating climate data. Remote Sensing 2021; 13(3): 484.

Zaini N, Yanis M, Abdullah F, Van Der Meer F, Aufaristama M. Exploring the geothermal potential of Peut Sagoe volcano using Landsat 8 OLI/TIRS images. Geothermics 2022; 105: 102499.

Zhang S, Xiao K, Carranza EJM, Yang F. Maximum entropy and random forest modeling of mineral potential: Analysis of gold prospectivity in the Hezuo–Meiwu district, west Qinling Orogen, China. Natural Resources Research 2019; 28: 645-664.

Zhang X, Chan NW, Pan B, Ge X, Yang H. Mapping flood by the object-based method using backscattering coefficient and interference coherence of Sentinel-1 time series. Science of the Total Environment 2021; 794: 148388.

Zhao F, Peng Z, Qian J, Chu C, Zhao Z, Chao J, Xu S. Detection of geothermal potential based on land surface temperature derived from remotely sensed and in-situ data. Geo-spatial Information Science 2023; 1-17.

Zurqani HA, Post CJ, Mikhailova EA, Schlautman MA, Sharp JL. Geospatial analysis of land use change in the Savannah River Basin using Google Earth Engine. International journal of applied earth observation and geoinformation 2018; 69: 175-185.